Simulation of Czochralski Melt Flows Using Parallel Adaptive Finite Element Procedures

Dan Givoli* **Joseph E. Flaherty**

Department of Computer Science

Rensselaer Polytechnic Institute, Troy, NY 12180

Mark S. Shephard

Scientific Computation Research Center

Rensselaer Polytechnic Institute, Troy, NY 12180

July 14, 1996

*On leave from the Department of Aerospace Engineering, Technion — Israel Institute of Technology, Haifa 32000, Israel

Mailing address:

Before Aug. 1, 1996:

Prof. Dan Givoli
Dept. of Computer Science
Rensselaer Polytechnic Institute (RPI)
Troy, NY 12180

Tel. (518) 276-8713
Fax: (518) 276-4886, 276-4033
e-mail: givolid@cs.rpi.edu

After Aug. 1, 1996:

Prof. Dan Givoli
Dept. of Aerospace Engineering
Technion
Haifa 32000
ISRAEL

Tel. 972-4-293814
Fax: 972-4-231848
e-mail: aer7501@vmsa.technion.ac.il

Abstract

Simulation of steady-state and transient melt flows in a Czochralski (CZ) crystal growth process is performed. To this end, a new three-dimensional finite element scheme is developed, that is based on a Galerkin Least-Squares (GLS) space-time variational formulation, with capabilities which include general unstructured mesh generation, automatic adaptive mesh refinement and coarsening, and parallel implementation with automatic load-balancing. Numerical results are obtained for flows in silicon and indium phosphide (InP) melts, with or without a viscous encapsulant, in crucibles with a flat or curved bottom. The effects of natural convection due to buoyancy, forced convection due to crystal and crucible rotations, and their combination, are considered.

Keywords: Crystal growth, Czochralski, Finite element, Parallel, Adaptive, Galerkin Least Squares.

1. Introduction

Single crystals with specific electrical, mechanical and optical properties are required for some high-performance electronic and opto-electronic devices. Crystal applications include semiconductors, laser modulators, electromechanical transducers and solar panels. Techniques for bulk crystal growth with good quality control have improved dramatically in the last 40 years [1, 2], but nonetheless, full understanding of crystal growth processes is lacking, and new techniques or modifications of existing techniques are constantly under development. In this light, mathematical and numerical modeling of different growth processes play an important role in the design and optimization of crystal growth techniques.

One of the most popular bulk crystal growth techniques, with wide applications to semiconductors, is the Czochralski method (CZ) [3], illustrated in Fig. 1. This method is based on pulling the crystal from the melt. A rod holding an oriented seed is lowered to the surface of the melt contained in a crucible, and, after a solid crystal with the desired diameter is initiated, the rod is slowly pulled upwards. The crucible is externally heated in a controlled manner, to maintain the upper surface near the melting temperature and the crucible walls at a higher temperature. Large-diameter silicon crystals can be grown in this manner at a rate of a few centimeters per hour.

The main flow mechanism that is observed in the melt of a CZ process is that of natural convection due to buoyancy. In many cases the crystal and/or the crucible are rotated to increase the uniformity of the process and, thus, of the resulting crystal. In these cases, forced convection is combined with natural convection [4]. Additional effects such as the surface tension forces at the free surface of the melt, the shape of the melt-crystal interface, and heat radiation, also affect flow patterns in the melt [1].

The growth of III-V compound crystals, such as indium phosphide (InP), which is used mainly to provide substrates for electro-optical devices, is currently much more difficult than that of silicon, in terms of yield and quality control [5]–[7]. The CZ process is modified in this case to include a layer of a highly viscous encapsulant, such as B_2O_3, above the free surface of the melt to prevent evaporation of volatile components of the compound at the melt surface.

This modified process is called Liquid Encapsulated Czochralski (LEC) growth (see Fig. 1). In some of the modern systems, a high-pressure gas is contained in the growth chamber above the encapsulant, to further suppress the separation of the volatile components from the melt. A magnetic field may be applied as well (MLEC) to decrease flow fluctuations in the melt [5]–[7].

The complete modeling of high-pressure LEC growth is thus extremely complex. It involves a multiphase system in which the melt, crystal, encapsulant, gas, crucible and chamber walls, all interact with each other, and where the shapes of several interfaces are not known a-priori [8, 9]. The cited flow mechanisms may give rise to different physical instabilities, including Rayleigh-Bénard convection (onset of buoyancy-driven convection), classical Bénard convection (driven by surface tension effects), loss of axial symmetry, and transition from steady to unsteady flow [10].

There have been many attempts to model various crystal growth systems with various levels of complexity (see, e.g., [11, 9]). Numerical methods include the use of finite volume [12]–[14], finite difference [15, 16], spectral [17], and finite element [18], [19]–[22] schemes.

In the present paper, we utilize a new finite element framework to perform the simulation of CZ and LEC flows. The scheme is designed to perform large-scale three-dimensional analysis of viscous flows, and in particular, to solve the Navier-Stokes equations with the Boussinesq approximation. The numerical aspects of this scheme are discussed in detail in [23]. It is based on a Galerkin Least-Squares (GLS) space-time variational formulation. Unstructured spatial meshes of tetrahedral elements are employed, with linear spatial interpolation in all variables. Piecewise-constant interpolation is used in time, with local time-stepping for steady flows. The scheme incorporates automatic adaptive mesh refinement, with a choice of various error indicators. The code runs on a distributed-memory MIMD parallel computer, and includes automatic load-balancing and data migration procedures. The nonsymmetric system of algebraic equations is solved iteratively using GMRES.

The long-term goal of this effort is to apply this new methodology to global CZ, LEC

and MLEC crystal growth simulations. In this paper, we consider the melt independently of the other phases. However, the current single-phase simulation is intended to be one of the ingredients in a coupled multiphase time-dependent analysis of an InP high-pressure crystal growth system, currently under development.

In the next section, we define the CZ/LEC model under consideration. In Section 3, we discuss the finite element formulation used. In Section 4, we briefly review the general solution framework and its various ingredients, including the parallel adaptive environment. In Section 5, we present the results of the simulation. We consider flows in silicon and InP melts, with or without a viscous encapsulant, in crucibles with a flat or curved bottom. The simulation accounts for the effects of natural convection due to buoyancy, forced convection due to crystal and crucible rotations, and their combination. We close the paper with some remarks.

2. Mathematical Model

We consider the three-dimensional flow in a crystal melt contained in a crucible, in a CZ or LEC configuration (see Fig. 1). The crucible is cylindrical, with radius r_c and height H, possibly with a non-flat bottom. We introduce a cylindrical system of coordinates (r, θ, z), with the z axis coinciding with the crucible axis and pointing upwards. We assume that the entire top surface of the melt (including the crystal-melt interface and the melt free surface or melt-encapsulant interface) is planar. The solid-melt interface is assumed to be circular with radius r_s. In addition to natural convection due to buoyancy, forced convection may take place due to rotation of the crucible with angular velocity ω_c, and/or rotation of the solid crystal with angular velocity ω_s.

We denote the three-dimensional melt domain by Ω, the part of the boundary of Ω defined by the crucible walls and bottom by Γ_c, the melt-solid interface by Γ_s, and the free surface of the melt (or the melt-encapsulant interface) by Γ_f. The entire boundary of Ω is $\Gamma \equiv \Gamma_c \cup \Gamma_s \cup \Gamma_f$. The governing equations in Ω are the Navier-Stokes equations with the

Boussinesq approximation [24],

$$\rho_0 \left(\dot{\boldsymbol{v}} + \boldsymbol{v} \cdot \nabla \boldsymbol{v} \right) = \nabla \cdot \boldsymbol{\sigma} + \rho_0 \beta g \left(T - T_0 \right) \boldsymbol{e}_z \ , \tag{1}$$

$$\nabla \cdot \boldsymbol{v} = 0 \ , \tag{2}$$

$$\rho_0 c_p \left(\dot{T} + \boldsymbol{v} \cdot \nabla T \right) - \nabla \cdot (\kappa \nabla T) = 0 \ . \tag{3}$$

Here, $\boldsymbol{v}$ is the velocity vector, T is the temperature, $\boldsymbol{\sigma}$ is the stress tensor, ρ_0 is a constant reference density of the fluid, T_0 is a reference temperature (chosen to be the melting temperature T_{mp}), β is the thermal expansivity of the fluid, g is the gravitational acceleration, $\boldsymbol{e}_z$ is a unit vector in the z direction, c_p is the heat capacity, and κ is the heat conductivity of the fluid. A superposed dot indicates differentiation with respect to time. Eqs. (1), (2) and (3) are, respectively, the momentum, continuity and energy equations. The last term on the right side of (1) is the buoyancy term, which is responsible for the coupling between the temperature and the velocity fields. The stress-pressure-velocity relations are given by

$$\boldsymbol{\sigma} = -p\boldsymbol{I} + \mu(\nabla \boldsymbol{v} + \nabla \boldsymbol{v}^T) \ , \tag{4}$$

where $\boldsymbol{I}$ is the identity tensor, and μ is the fluid viscosity.

The boundary conditions considered are

$$T = T_c \ ; \qquad v_r = v_z = 0 \ , \qquad v_\theta = \omega_c r \ , \qquad \text{on} \quad \Gamma_c \tag{5}$$

$$T = T_{mp} \ ; \qquad v_r = v_z = 0 \ , \qquad v_\theta = \omega_s r \ , \qquad \text{on} \quad \Gamma_s \tag{6}$$

$$q_z = -\kappa \partial T / \partial z = 0 \ ; \qquad v_z = 0 \ , \qquad \text{on} \quad \Gamma_f \tag{7}$$

$$\text{CZ} : \qquad \sigma_{zr} = \sigma_{z\theta} = 0 \ , \qquad \text{on} \quad \Gamma_f \tag{8}$$

$$\text{LEC:} \qquad v_r = 0 \ , \qquad v_\theta = V_{CF}(r) \ , \qquad \text{on} \quad \Gamma_f \tag{9}$$

with the following interpretation. On the walls and bottom of the crucible (Γ_c), a no-slip condition and a given constant temperature T_c are prescribed. On the solid-melt interface (Γ_s), a no-slip condition is applied, and the temperature is equal to the melting-point temperature T_{mp}. In the case of CZ flows, where no encapsulant is present, zero normal velocity and zero shear stress (free-slip) conditions are imposed on Γ_f. In the case of LEC flows,

no-slip conditions are imposed on Γ_f. In both cases, zero normal heat flux is assumed. If the crucible and/or crystal rotate, the no-slip conditions imply rotation of the fluid with angular velocity ω_c and/or ω_s on the corresponding boundaries. In the case of LEC flow with crucible and/or crystal rotation, the motion of the encapsulant (and hence that of the melt-encapsulant interface) is assumed to be in accordance with the classical Couette flow velocity distribution (flow between two long concentric rotating cylinders), namely,

$$v_\theta = V_{CF}(r) \equiv Ar + \frac{B}{r} , \qquad \text{on} \quad \Gamma_f , \tag{10}$$

where

$$A = \frac{\omega_c r_c^2 - \omega_s r_s^2}{r_c^2 - r_s^2} , \qquad B = \frac{(\omega_s - \omega_c) r_c^2 r_s^2}{r_c^2 - r_s^2} . \tag{11}$$

This assumed velocity distribution on the melt-encapsulant interface is reasonable since the encapsulant is much more viscous than the melt. A more accurate model necessitates accounting for the flow in the encapsulant itself.

The initial conditions are

$$T \equiv T_c , \qquad \boldsymbol{v} \equiv \mathbf{0} , \qquad \text{at} \quad t = 0 . \tag{12}$$

Thus, at time $t = 0^+$ there is a sudden change in the temperature of the crystal-melt interface Γ_s, from T_c to T_{mp}.

The equations, boundary and initial conditions given above can be non-dimensionalized in a number of ways. For later reference, we define four non-dimensional parameters [4]. The Grashof number, which is the ratio of buoyancy to viscous forces, is

$$\mathrm{Gr} = \rho_0^2 \beta g r_c^3 (T_c - T_{mp})/\mu^2 . \tag{13}$$

The Reynolds numbers associated with the crucible and crystal rotation, are, respectively,

$$\mathrm{Re_c} = \omega_c \rho_0 r_c^2/\mu , \qquad \mathrm{Re_s} = \omega_s \rho_0 r_c^2/\mu . \tag{14}$$

Finally, the Prandtl number, $\mathrm{Pr} = \mu c_p/\kappa$, as usual.

3. Finite Element Formulation

To simplify the presentation, we rewrite equations (1)–(3) in the vector form,

$$\dot{\boldsymbol{U}} + \mathcal{L}\boldsymbol{U} = \boldsymbol{S}_0 \ , \tag{15}$$

where $\boldsymbol{U}$ is the 5-dimensional vector of unknown variables, $\mathcal{L}$ is a differential operator, and $\boldsymbol{S}_0$ is a constant vector. We define a weak form of (15) based on the time-discontinuous Galerkin Least Squares (GLS) method. This formulation was originally developed for two-dimensional compressible flows [25], was later extended to three-dimensional inviscid flows and incorporated into a parallel adaptive computing environment [26], and was recently applied to two-dimensional incompressible flows, by taking the incompressible limit [27, 28]. Here we extend the formulation used in [26] to the solution of equations (1)–(3), or (15).

First we introduce some notation. Given a spatial domain Ω, consider a space-time domain $\Omega \times I$, where the time interval I is divided into subintervals (time steps), $I_n = (t_n, t_{n+1})$. Let $Q_n = \Omega \times I_n$ define a "space-time slab." Also, let $\boldsymbol{W}_n^-$ and $\boldsymbol{W}_n^+$ denote the values of the time-discontinuous quantity $\boldsymbol{W}$ as $t \to t_n$ from below and above, respectively. The slab Q_n is decomposed into $(N_{el})_n$ space-time elements, denoted Q_n^e. Finally, let $\mathcal{S}(Q_n)$ and $\mathcal{S}_0(Q_n)$ denote the appropriate trial and test spaces, respectively, defined on the slab Q_n.

With this notation, the variational formulation of (15) is stated as follows: within each slab Q_n, find $\boldsymbol{U} \in \mathcal{S}(Q_n)$ such that for all $\boldsymbol{W} \in \mathcal{S}_0(Q_n)$,

$$\begin{aligned} &\int_{Q_n} \left(-\dot{\boldsymbol{W}} \cdot \boldsymbol{U} + \boldsymbol{W} \cdot (\mathcal{L}\boldsymbol{U} - \boldsymbol{S}_0) \right) dQ \\ &+ \int_{\Omega} \left(\boldsymbol{W}_{n+1}^- \cdot \boldsymbol{U}_{n+1}^- - \boldsymbol{W}_n^+ \cdot \boldsymbol{U}_n^- \right) d\Omega \\ + \sum_{e=1}^{(N_{el})_n} &\int_{Q_n^e} (\mathcal{L}\boldsymbol{W}) \cdot \boldsymbol{\tau} \, (\mathcal{L}\boldsymbol{U} - \boldsymbol{S}_0) \, dQ = 0 \end{aligned} \tag{16}$$

The first integral in (16) is the standard Galerkin term. It is implemented in an integrated-by-parts form, resulting in an additional boundary integral [23]. The second integral weakly enforces continuity of the solution in time from one slab to the next. The first and second

integrals together constitute the discontinuous-Galerkin method [29]. The third integral in (16) is a stabilizing least squares (LS) term. The variational form (16) constitutes the time-discontinuous GLS method. Essential and natural boundary conditions can be applied in conjunction with (16) [23].

The matrix τ appearing in the LS term in (16) is designed to balance stability and accuracy in both the diffusive and advective limits. Definitions of τ for the compressible and incompressible Navier-Stokes equations can be found in [25] and [30], respectively. A way to construct a uniform τ is proposed in [28]. As can be seen from (16), the LS operator is applied at the element level. The method is consistent in the sense that (16) is satisfied by the exact solution of the problem.

4. Solution Procedures

The finite element code incorporates the time-discontinuous GLS formulation (16) in a computational environment that includes several special features [31]. Some of these were originally developed for large-scale aerodynamic compressible Euler calculations [32, 26], and have been extended to incompressible viscous buoyancy-driven flows. These features include:

• *General unstructured meshes of tetrahedral elements.* Spatial meshes are generated via the Finite Octree technique [33], which has proved to be an extremely strong tool for general three-dimensional geometries. Mesh generation and refinement are performed in conjunction with a parallel/adaptive environment [34, 31].

• *Special procedure for specifying the physical attribute information* required to support the analysis (e.g., boundary conditions) [35, 31].

• *Piecewise-constant interpolation in time; local time-stepping for steady flows.* In steady-state analysis, we march rapidly in time to reach a steady state. In this case, the time-step need not be uniform throughout the mesh, but is determined locally, to achieve a specified element Courant number. In a time-dependent analysis, a uniform time-step (possibly varying with time) is specified.

• *Continuous piecewise-linear spatial interpolation in all the variables.* This convenient choice is made possible by the LS stabilization.

• *Iterative solution of the nonsymmetric algebraic linear system via preconditioned GMRES.*

• *Parallel implementation, with an automatic load balancing procedure.* The present finite element scheme is designed to work in an automatic parallel adaptive environment. Special strategies and procedures are used for (a) partitioning of data among the processors, (b) data exchange among processors, (c) efficient parallel implementation of the matrix-vector multiplications and vector dot products involved in the GMRES solver, (d) fast query and update of partition boundary information needed for the refinement/coarsening and element migration/load balancing, and (e) the migration of elements among the processors to redistribute the mesh and restore load balance. For the latter task, an element-based dynamic load balancing scheme is used, which iteratively migrates elements from heavily loaded to less loaded processors (see [23], [31], [32] and [36]).

These parallel procedures result in a scalable code that runs on a distributed-memory MIMD parallel computer. The simulations described in Section 5 are performed on an IBM SP-2 computer, at Rensselaer Polytechnic Institute (36 processors), and at Cornell University (512 processors).

• *Automatic adaptive mesh refinement/coarsening with various error indicators.* The adaptive procedure enables effective resolution of boundary layers and large-gradient regions. The error indicators available involve the magnitude of either the first or second derivatives of the solution, and can be applied to one or more physical variables (temperature, velocity, etc.) [23]. In time-dependent analysis, an initial mesh is generated at time $t = 0$, and a mesh adaptation step is performed after a prescribed number of time-steps, using the chosen error indicator. In steady-state analysis, we first generate an initial mesh and then perform local time-stepping with this mesh, until the residual norm is reduced below a specified level, indicating that a steady state has been reached. Then, one step of mesh adaptation is performed, using the chosen error indicator. After this step, another cycle of local time stepping is performed until steady state is reached again. This procedure is repeated for a

desired number of cycles.

The mesh level adaptive scheme combines local refinement, coarsening and triangulation optimization using local retriangulations. These procedures are fully compatible with the parallel framework. After each iteration of triangulation optimization, a load balancing step is applied. Details on the procedures used, and their parallel implementation, are given in [23], [31] and [34].

5. Numerical Results

The finite element scheme is applied to the CZ melt flow problem described mathematically in Section 2. We consider two cases: silicon melt with no encapsulant (CZ) in a large cylindrical crucible, and InP melt with encapsulant (LEC) in a smaller crucible with a curved bottom. Table 1 lists the parameter values used in each case. The effects of buoyancy, crystal and crucible rotation are considered. We control the Gr, $\mathrm{Re_c}$ and $\mathrm{Re_s}$ numbers (see (13) and (14)) by assigning appropriate values to the crucible wall temperature, T_c, and to the crucible and crystal angular velocities, ω_c and ω_s.

Although our finite element scheme solves three-dimensional problems, the results shown here are axisymmetric. Both experimental evidence and numerical calculations with realistic value of Gr, show that CZ and LEC processes always involve flows which are time-dependent and fully three-dimensional [10, 16]. For Case 1 in Table 1 (silicon) with buoyancy-driven flows, transition to time-dependent three-dimensional solutions occurs at $\mathrm{Gr} \approx 5 \cdot 10^6$ [18, 14]. The extension of the current methodology to this regime is currently underway. Preliminary results, presented at the end of this section, look promising.

The flow problems are solved using 8, 16 and 32 parallel processors. The adaptive procedure described in Section 4 is used with an error indicator based on a combination of the magnitudes of the temperature and velocity gradients. One full Newton iteration is performed at each time step. The dimension of the Krylov space used in the GMRES solver is chosen to be 25.

We start with steady-state CZ melt flow of silicon in a large cylindrical crucible (Case

1 in Table 1). Local time-stepping is used to rapidly reach steady-state. Fig. 2(a) shows the initial mesh used for this simulation. It consists of about 140,000 tetrahedral elements. Fig. 2(b) shows a vertical cross section through the final mesh, obtained after two adaptive refinements. Mesh refinement near the walls of the crucible, and especially near the top boundary, is apparent. The final mesh consists of close to 400,000 elements, and a similar number of degrees of freedom.

In Fig. 3, the finite element results are shown for buoyancy driven flow, with $\mathrm{Gr}=5.6 \cdot 10^5$. The colors represent the temperature field, and the arrows represent the velocity field, projected onto a plane. Here, and elsewhere, the arrow lengths are proportional to the velocity magnitudes, although different scalings may be used in different figures, for clear visualization. Figs. 3(a) and 3(b) show the results on the vertical yz plane, and at the horizontal top plane ($z = H$), respectively. These results agree with those obtained in [18, 14]. At the heated vertical wall of the crucible the melt rises due to buoyancy, and then turns radially inwards at the melt surface. This gives rise to the Rayleigh-Bénard toroidal cell flow seen in Fig. 3(a). No flow is seen in Fig. 3(b) on the melt-crystal interface (the inner circle), due to the no-slip condition imposed on this surface.

Next, consider the LEC melt flow of InP in a small crucible with a curved bottom (Case 2 in Table 1). First we consider the steady-state flow. Fig. 4(a) shows the initial mesh used, and Fig. 4(b) shows the final mesh, obtained after two adaptive refinements. Again, the mesh is refined near the walls of the crucible, and especially near the top boundary. The asymmetric refinement seen in the final mesh is the result of small perturbations in the error indicator near the specified threshold, which exist in some regions. However, asymmetry in the mesh does not lead to significant asymmetry in the solution. The final mesh consists of close to 200,000 elements.

Fig. 5 shows the finite element results, in a vertical plane, for buoyancy-driven flow. Figs. 5(a), (b) and (c) correspond to $\mathrm{Gr}=3.3 \cdot 10^4$, $3.3 \cdot 10^5$ and 10^6, respectively. These results are similar in principle to those presented in [21, 18]. The flow cell is closer to the crucible wall than to the cylindrical axis, as in the "bulk-flow" model of [21]. The isotherms for large Gr

(Fig. 5(c)) are "distorted," reflecting the relative importance of convective heat transfer.

Fig. 6 shows the velocity pattern in a vertical plane due to crystal rotation with $\mathrm{Re}_s = 360$. The flow is isothermal and Gr=0; thus no buoyancy is involved. The velocity at the top surface of the fluid is specified by (9), using the Couette flow distribution (10) and (11). The flow pattern is as observed experimentally in [4] and numerically in [21]. The rotating crystal acts as a centrifugal fan, sucking up fluid axially, spinning it up, and ejecting it tangentially. Thus, in addition to the main rotational flow in the horizontal plane, a secondary flow is generated in the vertical plane, which has the opposite sense to that of the buoyancy-driven flow (see Fig. 5).

Results in Fig. 7 show the flow in a vertical plane, with both buoyancy with $\mathrm{Gr}=3.3 \cdot 10^5$ and crystal rotation with $\mathrm{Re}_s = 360$. Two flow cells with opposite sense are clearly visible; the lower one is the buoyancy cell, whereas the upper one is smaller and is generated by the crystal rotation. The interaction of natural and forced convection is highly nonlinear.

Fig. 8 shows results with the combined effects of buoyancy ($\mathrm{Gr}=3.3 \cdot 10^5$), crystal rotation ($\mathrm{Re}_s = 360$) and crucible rotation ($\mathrm{Re}_c = 110$). The crystal and crucible rotate in the same sense, in this example.

The characteristics of these solutions are similar to those reported in [21], [18] and [4]. We note, however, that these results are expected to differ significantly from those obtained in a fully-coupled LEC simulation. This has been demonstrated in [21], where the results of a simple CZ "bulk-flow" model and of a coupled thermal-capillary model were compared in various configurations. The significant differences in the results of the two models, especially at high Gr numbers, show that flow coupling effects are important, and thus the uncoupled model is too simple to yield accurate information.

We next apply the finite element scheme to a time-dependent process with the parameters of Case 2 of Table 1. The process is described as follows: First, steady buoyancy-driven flow with $\mathrm{Gr}=3.3 \cdot 10^5$ is considered (see Fig. 5(b)). Crystal rotation with $\mathrm{Re}_s = 360$ is started (at $t = 0$) and the evolution of the flow is followed, until a second steady state is reached (see Fig. 7).

We initiate the computational process with the final mesh and solution of the steady-state flow with Gr=$3.3 \cdot 10^5$ (Figs. 4(b) and 5(b)). Then, we start crystal rotation with $\mathrm{Re}_s = 360$, and march in time, using a constant time step of 0.01 seconds throughout the mesh. At times $t = 2$ and $t = 8$, we perform a step of mesh adaptation, using a combination of the magnitudes of the temperature and velocity gradients of the current solution as an error indicator. We march until $t = 110$ sec., which we take as steady state.

Figs. 9(a), (b) and (c) show, respectively, the finite element results at times $t = 4$, $t = 8$ (just before the second adaptive step), and $t = 17$. The crystal rotation has the effect of reversing the flow direction in the region near the crystal-melt interface. At $t = 4$ (Fig. 9(a)), the buoyancy-driven flow is almost stagnant below this interface, whereas at $t = 8$ (Fig. 9(b)), a small rotation cell has started to form. At $t = 17$ (Fig. 9(c)), the crystal-rotation flow cell becomes significantly larger. In fact, it is even slightly larger than that obtained at steady state (Fig. 7). This indicates a physical "overshoot" phenomenon. The crystal-rotation cell reaches a maximum size at about $t = 10$, and then starts to decrease, and approaches a steady state.

Figs. 10(a) and 10(b) show vertical sections through the meshes obtained at times $t = 2$ and $t = 8$, respectively. The mesh at $t = 2$ consists of about 315,000 elements, whereas the mesh at $t = 8$ contains over 410,000 elements. As the size of the upper flow cell increases, and the flow at the bottom of the crucible becomes stronger (see Fig. 9), additional regions of the mesh are refined during the adaptive steps. Thus, in Fig. 10(b) the refined area below the crystal-melt interface is deeper than that in Fig. 10(a), and additional refinement is observed at the bottom.

Finally, we consider buoynacy-driven flows with different Gr numbers. Time-dependent analysis is performed, with a constant time-step size of 0.05 seconds. Fig. 11 shows the variation of the total kinetic energy in time, for 6 values of Gr. The total kinetic energy is computed by summing the kinetic-energy density values $|\boldsymbol{v}|^2/2$ at all finite element integration points. Since this quantity is mesh-dependent, this computation has been performed with a fixed mesh. The energy curves shown in Fig. 11 are scaled independently, to fit into

the energy interval [0,100].

For Gr=$3.3 \cdot 10^5$, the energy curve is very smooth. An "overshoot" in the energy is observed as in the previous example. For Gr=$5 \cdot 10^6$ and $9.7 \cdot 10^6$, the energy is initially oscillatory, but rapidly approaches a constant value. Persistent oscillations are apparent for Gr= $1.4 \cdot 10^7$, $2.4 \cdot 10^7$ and $3.8 \cdot 10^7$. (We remark that some damping is observed for these values of Gr as well, but this is a numerical artifact due to the specific time integration used.) Thus, transition to unsteady flows occurs at about Gr = 10^7. The energy curves in the unsteady regime are characterized by short transient, followed by periodic oscillations with period of about 3.5 seconds. These results are consistent with those reported in [18], [37] and [13].

6. Concluding Remarks

We have described the simulation of steady-state and transient melt flows in Czochralski (CZ) and Liquid Encapsulated Czochralski (LEC) crystal growth processes, based on a single-phase uncoupled model. Simulations were performed using a new finite element scheme, that enables large-scale three-dimensional analysis of viscous flows. Full numerical details are given in [23]. Important features of the scheme include generation of general three-dimensional unstructured meshes, special procedures for specifying physical attributes, least-squares stabilization, local time-stepping for steady flows, parallel implementation, dynamic load balancing, and automatic adaptive mesh refinement/coarsening.

Further developments are currently underway, including a more efficient procedure for time-dependent analysis than that utilized for the preliminary study of Section 5. As noted, for realistic physical parameters, CZ and LEC processes are associated with three-dimensional transient flows. Effective time integration will be achieved using high-order singly implicit Runge-Kutta (SIRK) methods.

We intend to extend and apply the methodology described here to the coupled multiphase transient analysis of InP high-pressure crystal growth systems. The difficulties entailed in the realistic analysis of the full LEC system are mentioned in Section 1. We believe that the

current methodology serves as an excellent framework for such simulations. Progress in this direction will be reported in a future publication.

Acknowledgments

This work is partly supported by AFOSR, as part of the ARPA/AFOSR Consortium for Crystal Growth Research, under grant No. F49620-95-1-0407. The authors would also like to thank Dr. Carlo Bottasso, Dr. Simon Brandon, Prof. Leo Franca and Prof. Alex Ostrogorsky for their very helpful remarks.

References

[1] G. Müller, *Convection and Inhomogeneities in Crystal Growth from the Melt*, Crystals Vol. 12, Springer-Verlag, Berlin, 1988.

[2] D.T.J. Hurle, *Crystal Pulling from the Melt*, Springer-Verlag, Berlin, 1993.

[3] D.T.J. Hurle and B. Cockayne, "Czochralski Growth," in *Handbook of Crystal Growth*, D.T.J. Hurle, ed., Vol. 2A, Chap. 3, pp. 99–212, North-Holland, Amsterdam, 1994.

[4] G. Müller and A. Ostrogorsky, "Convection in Melt Growth," in *Handbook of Crystal Growth*, D.T.J. Hurle, ed., Vol. 2B, Chap. 13, pp. 709–819, North-Holland, Amsterdam, 1994.

[5] G.W. Iseler, "Advances in LEC Growth of InP Crystals," *J. Electronic Materials*, 13, 989–1011, 1984.

[6] G. Müller, J. Völkl and E. Tomzig, "Thermal Analysis of LEC InP Growth," *J. Crystal Growth*, 64, 40–47, 1983.

[7] V. Prasad, D.F. Bliss and J.A. Adamski, "Thermal Characterization of the High Pressure Crystal Growth System for In-situ Synthesis and Growth of InP Crystals," *J. Crystal Growth*, 142, 21–30, 1994.

[8] H. Zhang, V. Prasad and D.F. Bliss, "Modeling of High Pressure, Liquid-encapsulated Czochralski Growth of InP Crystals," *J. Crystal Growth*, 1996, to appear.

[9] F. Dupret and N. van den Bogaert, "Modelling Bridgman and Czochralski Growth," in *Handbook of Crystal Growth*, D.T.J. Hurle, ed., Vol. 2B, Chap. 15, pp. 875–1010, North-Holland, Amsterdam, 1994.

[10] Y. Yamaguchi, C.J. Chang and R.A. Brown, "Multiple Buoyancy-driven Flows in a Vertical Cylinder Heated from Below," *Phil. Trans. R. Soc. Lond.*, A312, 519–552, 1984.

[11] "Computer Modelling in Crystal Growth from the Melt" (paper collection), in *J. Crystal Growth*, Vol. 97, No. 1, 1–244, 1989.

[12] A. Anselmo, V. Prasad, J. Koziol and K.P. Gupta, "Oscillatory Convection in Low Aspect Ratio Czochralski Melts," *J. Crystal Growth*, 134, 116–139, 1993.

[13] H. Zhang and V. Prasad, "A Multizone Adaptive Process Model for Low and High Pressure Crystal Growth," *J. Crystal Growth*, 155, 47–65, 1995.

[14] A. Bottaro and A. Zebib, "Three Dimensional Thermal Convection in Czochralski Melt," *J. Crystal Growth*, 97, 50–58, 1989.

[15] G. Müller, G. Neumann and H. Matz, "A Two-Rayleigh-number Model of Buoyancy Driven Convection in Vertical Melt Growth Configurations," *J. Crystal Growth*, 84, 36–49, 1987.

[16] H. Kopetsch, "A Numerical Method for the Time-dependent Stefan Problem in Czochralski Crystal Growth," *J. Crystal Growth*, 88, 71–86, 1988.

[17] I. Raspo, J. Ouazzani and R. Peyret, "A Spectral Multidomain Technique for the Computation of the Czochralski Melt Configuration," *Int. J. Numer. Meth. Heat Fluid Flow*, 6, 31–58, 1996.

[18] M.J. Crochet, P.J. Wouters, F.T. Geyling and A.S. Jordan, "Finite Element Simulation of Czochralski Bulk Flow," *J. Crystal Growth*, 65, 153–165, 1983.

[19] P.A. Sackinger, R.A. Brown and J.J. Derby, "A Finite Element Method for Analysis of Fluid Flow, Heat Transfer and Free Interfaces in Czochralski Crystal Growth," *Int. J. Numer. Meth. Fluids*, 9, 453–492, 1989.

[20] S. Brandon and J.J. Derby, "Heat Transfer in Vertical Bridgman Growth of Oxides: Effects of Conduction, Convection, and Internal Radiation," *J. Crystal Growth*, 121, 473–494, 1992.

[21] Q. Xiao and J.J. Derby, "Bulk-flow Versus Thermal-capillary Models for Czochralski Growth of Semiconductors," *J. Crystal Growth*, 129, 593–609, 1993.

[22] J.J. Derby, S. Brandon, A.G. Salinger and Q. Xiao, "Large-scale Numerical Analysis of Materials Processing Systems: High-temperature Crystal Growth and Molten Glass Flows," *Comp. Meth. Appl. Mech. Engng.*, 112, 69–89, 1994.

[23] D. Givoli, J.E. Flaherty and M.S. Shephard, "Parallel Adaptive Finite Element Analysis of Viscous Flows with Application to Czochralski Melt Flows," *Int. J. Numer. Meth. Heat Fluid Flow*, 1996, submitted.

[24] B. Gebhart, Y. Jaluria, R.L. Mahajan and B. Sammakia, *Buoyancy-Induced Flows and Transport*, Hemisphere Publishing, Washington, 1988.

[25] F. Shakib, T.J.R. Hughes and Z. Johan, "A New Finite Element Formulation for Computational Fluid Dynamics: X. The Compressible Euler and Navier Stokes Equations," *Comp. Meth. Appl. Mech. Engng.*, 89, 141–219, 1991.

[26] C.L. Bottasso, H.L. de Cougny, M. Dindar, J.E. Flaherty, C. Ozturan, Z. Rusak and M.S. Shephard, "Compressible Aerodynamics Using a Parallel Adaptive Time-discontinuous Galerkin Least-Squares Finite Element Method," in *Proc. 12th AIAA Applied Aerodynamics Conference*, No. 94-1888, Colorado Springs, 1994, AIAA.

[27] G. Hauke and T.J.R. Hughes, "A Unified Approach to Compressible and Incompressible Flows," *Comp. Meth. Appl. Mech. Engng.*, 113, 389–395, 1994.

[28] G. Hauke, A unified Approach to Compressible and Incompressible Flows and A New Entropy-consistent Formulation of the $k - \epsilon$ Model, Ph.D. Dissertation, Stanford University, Stanford, 1995.

[29] C. Johnson, *Numerical Solutions of Partial Differential Equations by the Finite Element Method*, Cambridge University Press, Cambridge, 1987.

[30] L.P. Franca and S.L. Frey, "Stabilized Finite Element Methods: II. The Incompressible Navier-Stokes Equations," *Comp. Meth. Appl. Mech. Engng.*, 89, 141–219, 1992.

[31] M.S. Shephard, J.E. Flaherty, H.L. de Cougny, C. Ozturan, C.L. Bottasso and M.W. Beall, "Parallel Automated Adaptive Procedures for Unstructured Meshes," in *Parallel Computing in CFD*, Vol. R-807, pp. 6.1-6.49, AGARD, Nevilly-sur-Seine, France, 1995.

[32] M.S. Shephard, C.L. Bottasso, H.L. de Cougny and C. Ozturan, "Parallel Adaptive Finite Element Analysis of Fluid Flows on Distributed Memory Computers," in *Recent Developments in Finite Element Analysis*, eds. T.J.R. Hughes, E. Oñate and O.C. Zienkiewicz, pp. 205–214, Int. Center for Num. Meth. in Engng., Barcelona, Spain, 1994.

[33] M.S. Shephard and M.K. Georges, "Automatic Three-dimensional Mesh Generation by the Finite Octree Technique," *Int. J. Numer. Meth. Engng.*, 32, 709–749, 1991.

[34] C. Ozturan, H.L. de Cougny, M.S. Shephard and J.E. Flaherty, "Parallel Adaptive Mesh Refinement and Redistribution on Distributed Memory Machines," *Comp. Meth. Appl. Mech. Engng.*, 119, 123–137, 1994.

[35] M.S. Shephard, "The Specification of Physical Attribute Information for Engineering Analysis," *Eng. with Comp.*, 4, 145–155, 1988.

[36] H.L. de Cougny, K.D. Devine, J.E. Flaherty, R.M. Loy, C. Ozturan and M.S. Shephard, "Load Balancing for the Parallel Solution of Partial Differential Equations," *Appl. Numer. Math.*, 16, 157–182, 1994.

[37] A. Bottaro and A. Zebib, "Bifurcation in Axisymmetric Czochralski Natural Convection," *Phys. Fluids*, 31, 495–501, 1988.

Case	Material	CZ/LEC	Bottom	r_c [cm]	r_s [cm]	H [cm]
1	Silicon	CZ	flat	7.6	$r_c/2$	$2r_c$
2	InP	LEC	curved	3.4	$r_c/2$	r_c

Case	ρ_0 [g/cm^3]	μ [g/cm-s]	κ [W/cm-K]	c_p [J/g-K]	β [1/K]	T_{mp} [K]
1	2.53	0.0088	0.67	1.04	$1.32 \cdot 10^{-4}$	1683
2	5.05	0.0081	0.23	0.42	$4.44 \cdot 10^{-4}$	1335

Table 1. Parameter values used for the CZ/LEC melt flow simulations.

Captions for Figures

Fig. 1. Liquid Encapsulated Czochralski (LEC) process.

Fig. 2. CZ melt flow of silicon: finite element meshes. (a) Initial mesh, (b) vertical section through the final mesh.

Fig. 3. CZ melt flow of silicon: results for buoyancy-driven flow, $\mathrm{Gr}=5.6 \cdot 10^5$. Temperature variation and velocity pattern shown (a) in a vertical plane, (b) at the top horizontal plane, $z = H$.

Fig. 4. LEC melt flow of InP: finite element meshes. (a) Initial mesh, (b) final mesh.

Fig. 5. LEC melt flow of InP: temperature and velocity distributions for buoyancy-driven flow in a vertical plane. (a) $\mathrm{Gr}=3.3 \cdot 10^4$, (b) $\mathrm{Gr}=3.3 \cdot 10^5$, (c) $\mathrm{Gr}=10^6$.

Fig. 6. LEC melt flow of InP: flow due to crystal rotation in a vertical plane for $\mathrm{Re_s} = 360$ (Gr=0).

Fig. 7. LEC melt flow of InP: flow due to both buoyancy ($\mathrm{Gr}=3.3 \cdot 10^5$) and crystal rotation ($\mathrm{Re_s} = 360$). Temperature and velocity distributions in a vertical plane.

Fig. 8. LEC melt flow of InP: flow due to the combined effects of buoyancy ($\mathrm{Gr}=3.3 \cdot 10^5$), crystal rotation ($\mathrm{Re_s} = 360$) and crucible rotation ($\mathrm{Re_c} = 110$). Temperature and velocity distributions in a vertical plane.

Fig. 9. LEC melt flow of InP, time dependent analysis ($\mathrm{Gr}=3.3 \cdot 10^5$, $\mathrm{Re_s} = 360$): flow at (a) $t = 4$, (b) 8, (c) 17 sec., after start of crystal rotation. Temperature and velocity distributions are shown in a vertical plane.

Fig. 10. LEC melt flow of InP, time-dependent analysis (Gr=$3.3 \cdot 10^5$, $\mathrm{Re_s} = 360$): vertical section through adapted meshes used, (a) at $t = 2$, (b) 8 sec., after start of crystal rotation.

Fig. 11. LEC melt flow of InP, time-dependent analysis for buoyancy driven flow: scaled total kinetic energy as a function of time, for various values of Gr.

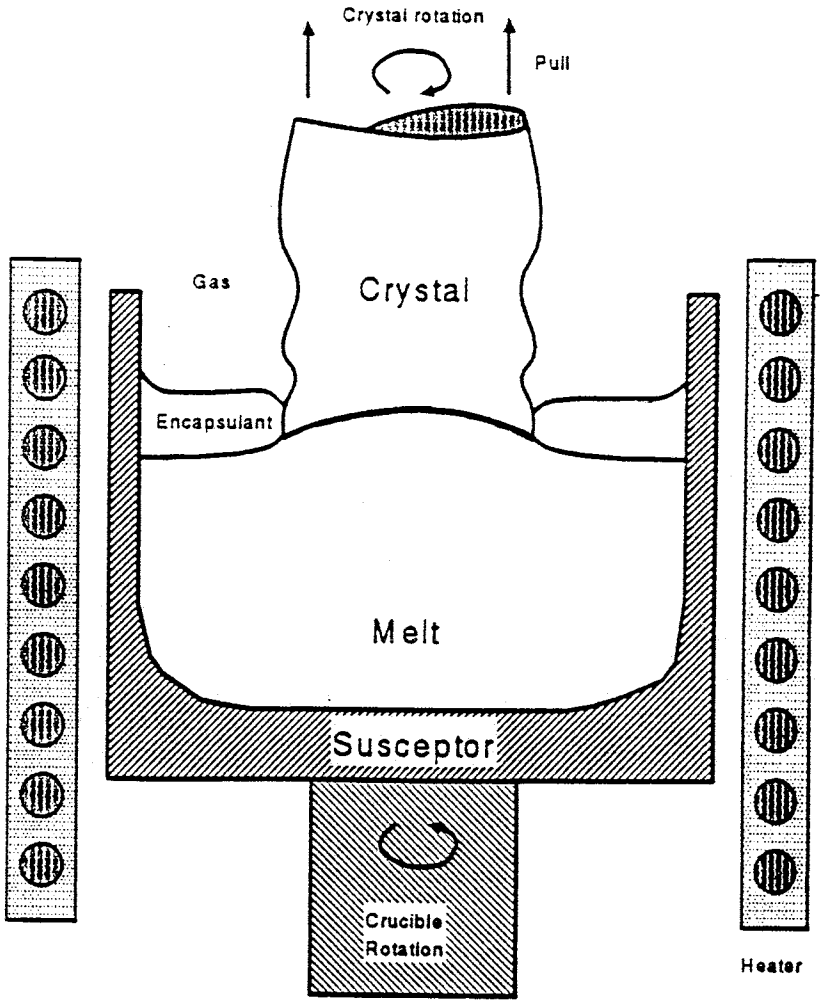
Crystal rotation
Pull
Gas
Crystal
Encapsulant
Melt
Susceptor
Crucible
Rotation
Heater

Fig. 1

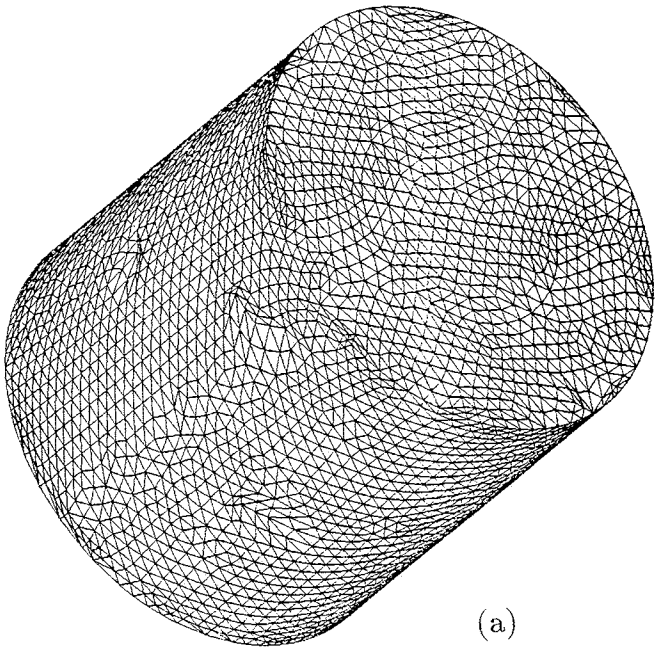

(a)

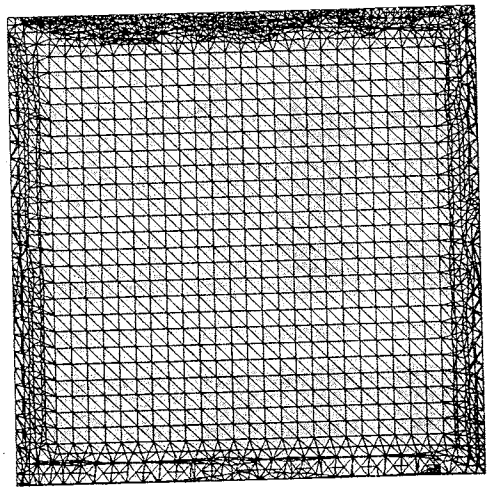

(b)

Fig. 2

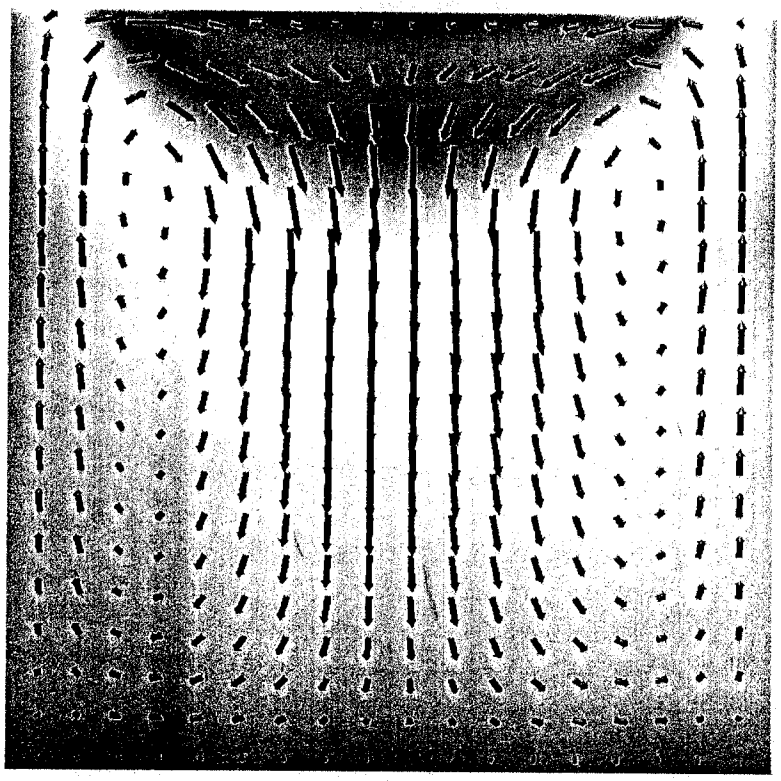

Fig. 3(a)

(color)

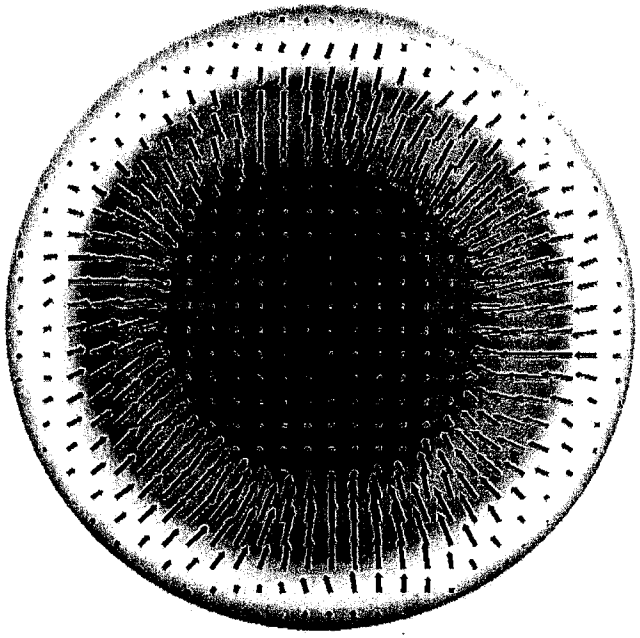

Fig. 3(b)

(Color)

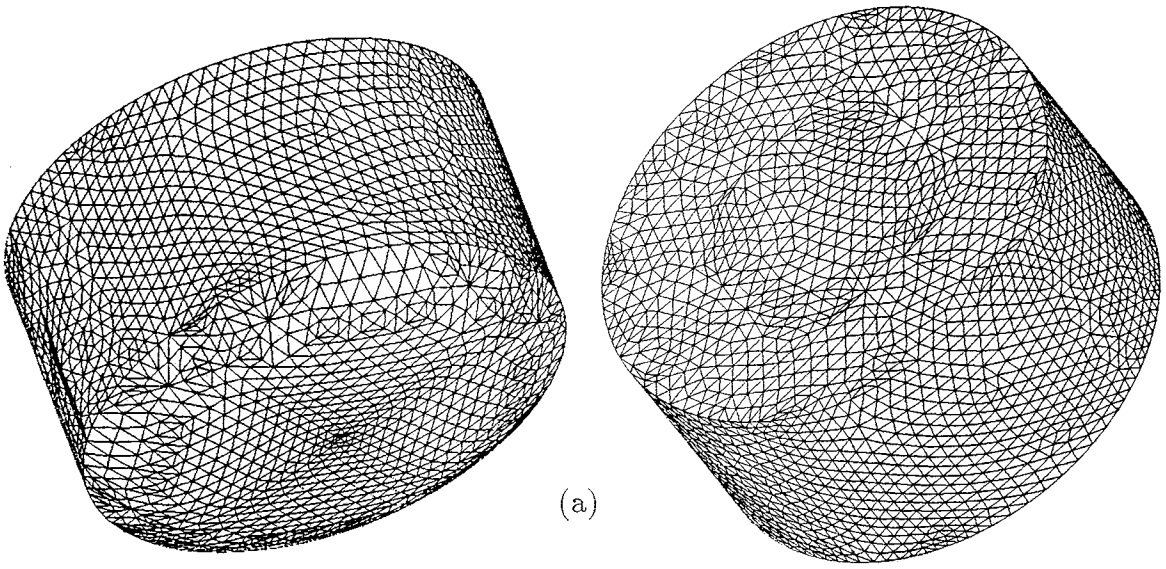

(a)

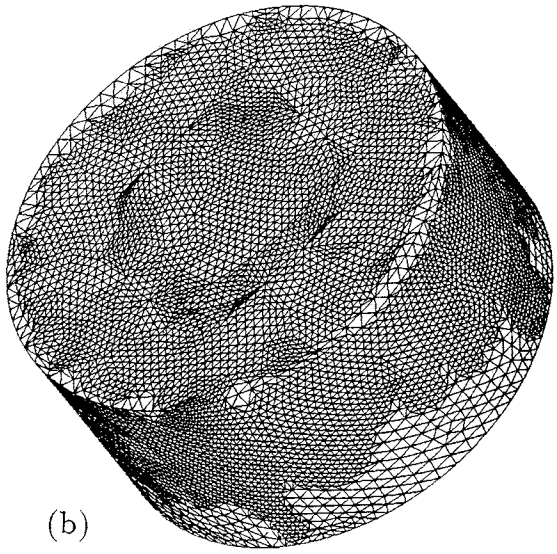

(b)

Fig. 4

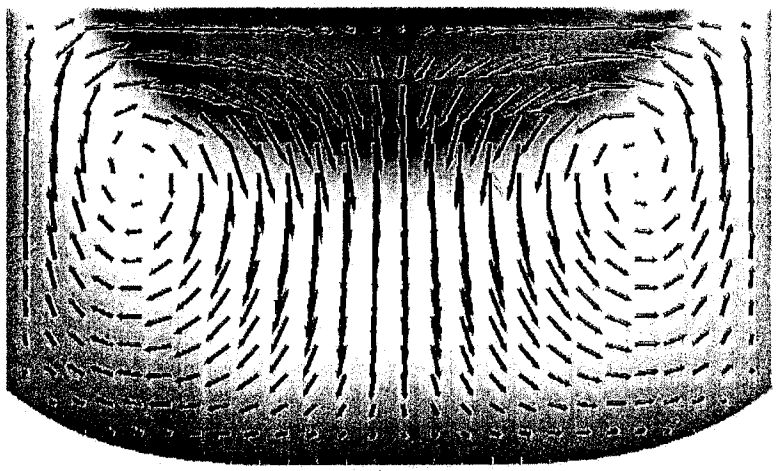

Fig. 5(a)

(Color)

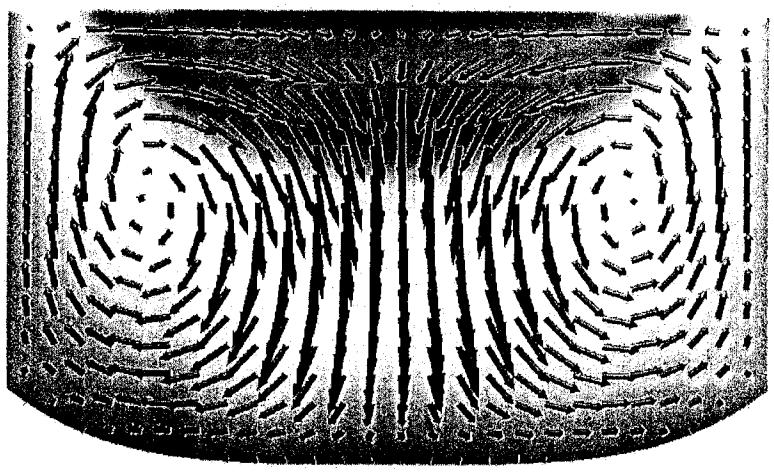

Fig. 5(b)

(Color)

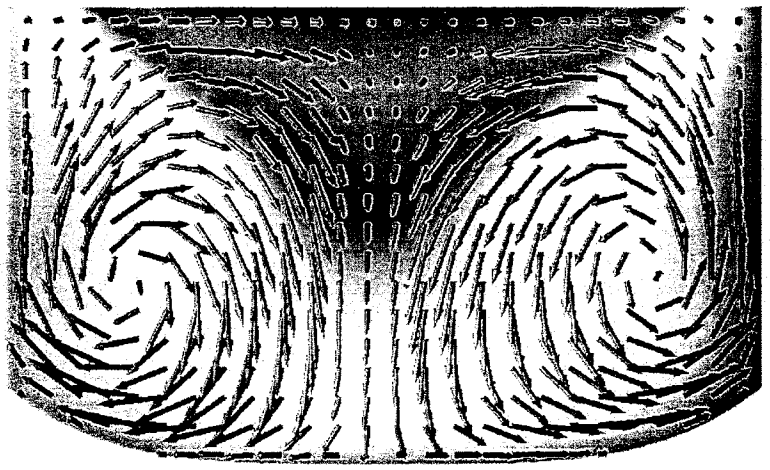

Fig. 5(c)

(color)

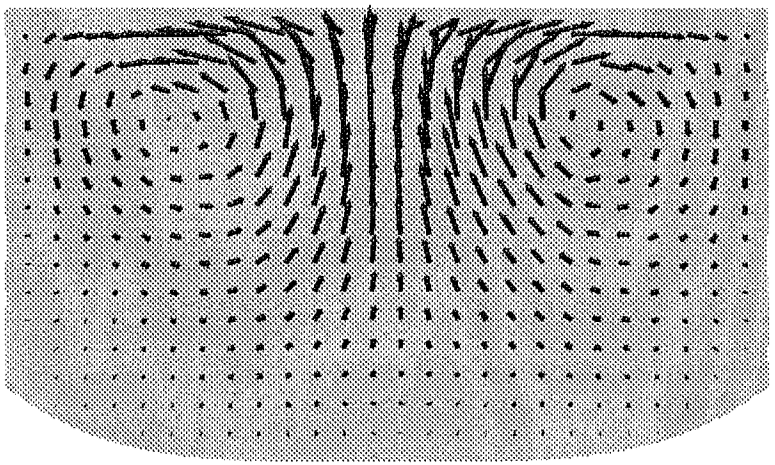

Fig. 6

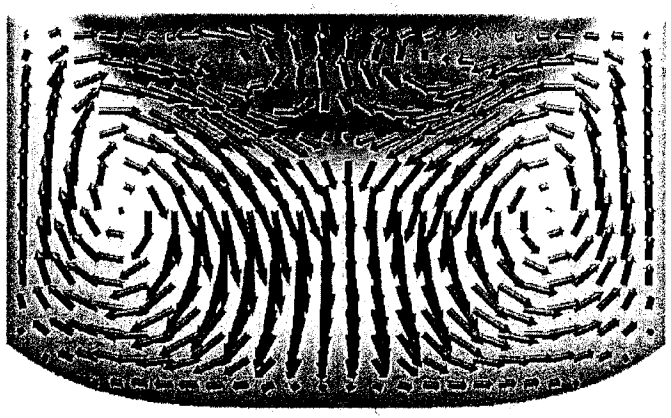

Fig. 7

(Color)

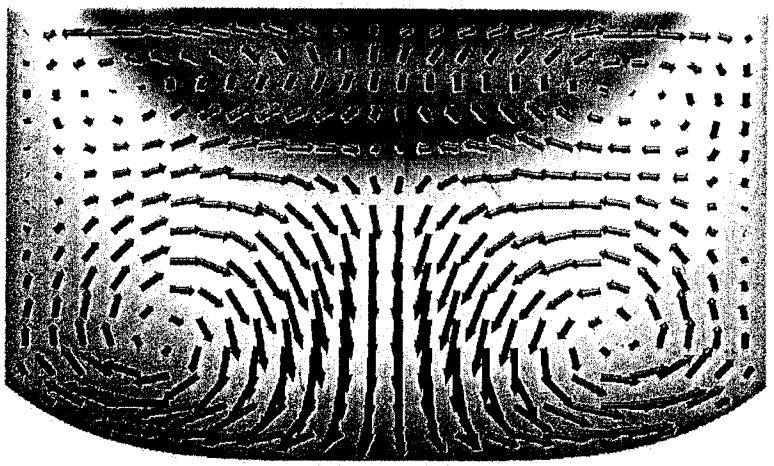

Fig. 8

(color)

Fig. 9(a)

Color

Color

Fig. 9(b)

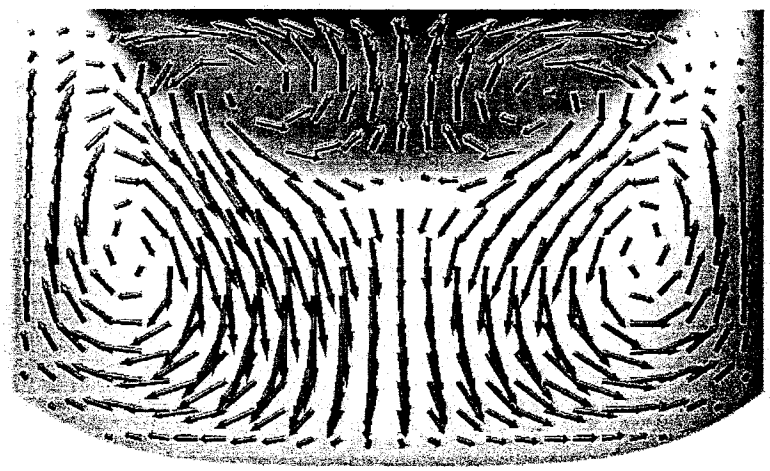

Color

Fig. 9(c)

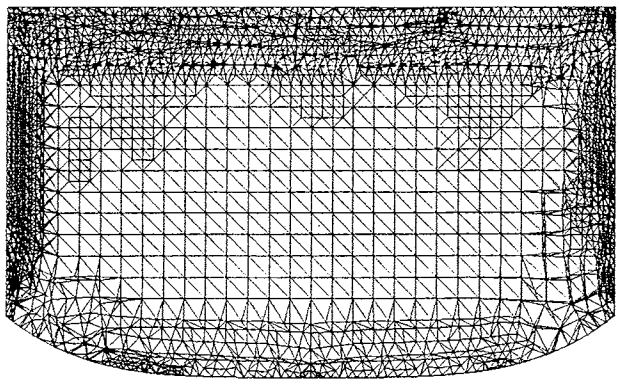

(a)

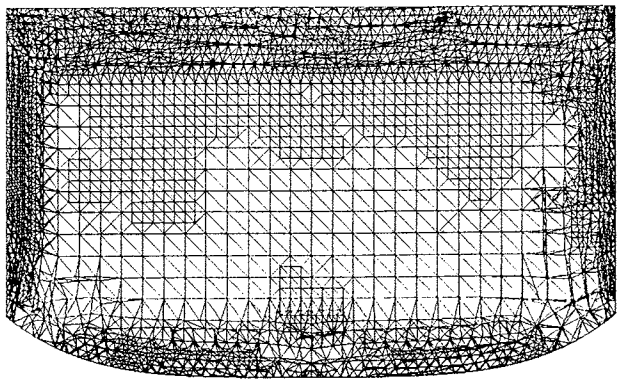

(b)

Fig. 10

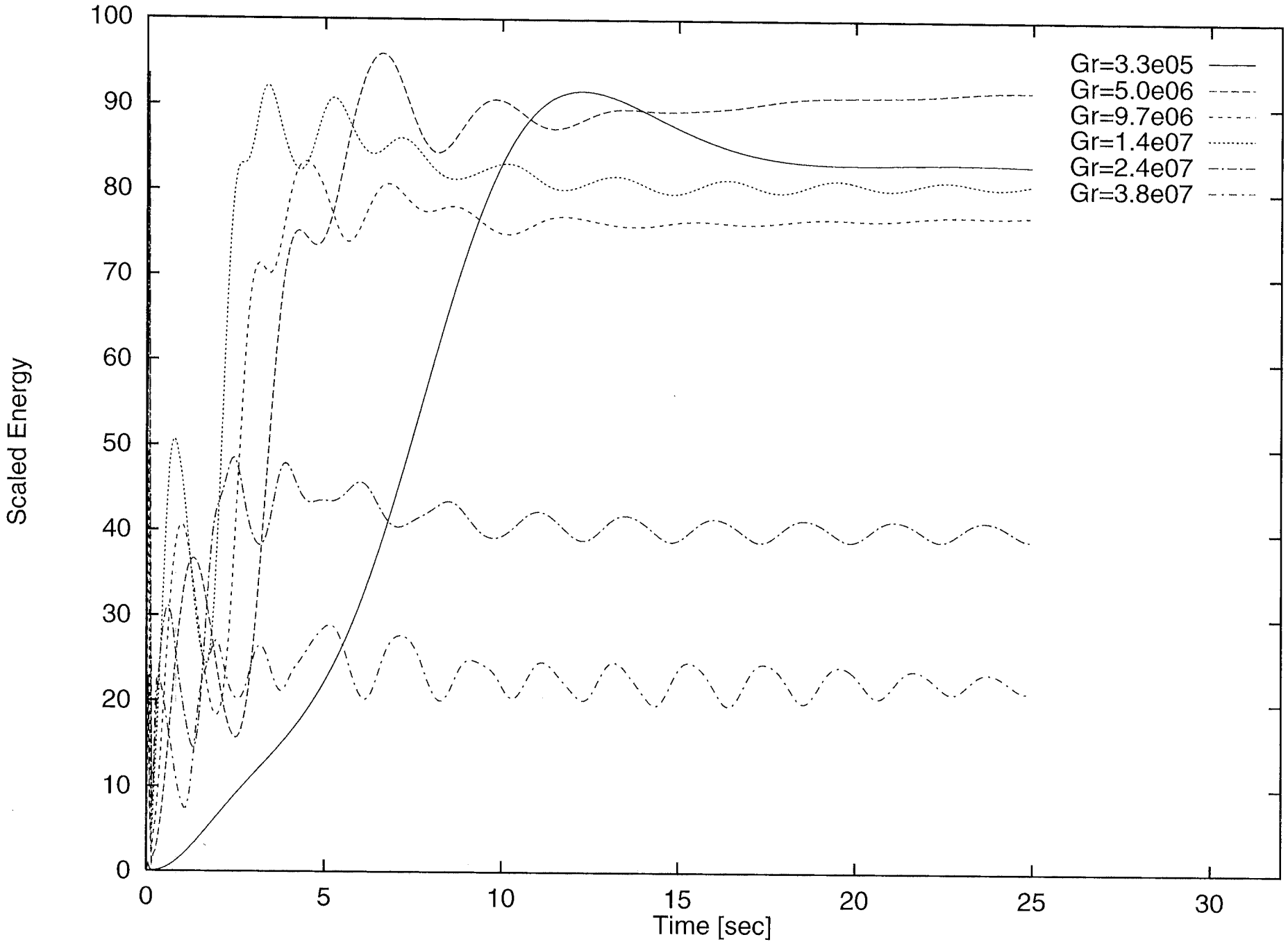
Scaled Energy
Time [sec]
Gr=3.3e05
Gr=5.0e06
Gr=9.7e06
Gr=1.4e07
Gr=2.4e07
Gr=3.8e07
0
10
20
30
40
50
60
70
80
90
100
0
5
10
15
20
25
30

Fig. 11